Low frequency earthquakes below southern Vancouver Island

M. G. Bostock, A. A. Royer, E. H. Hearn, and S. M. Peacock

Department of Earth, Atmospheric and Ocean Sciences, University of British Columbia, Vancouver, British Columbia V6T 1Z4, Canada (bostock@eos.ubc.ca)

[1] The nature and distribution of low frequency earthquakes (LFEs) in subduction zones provide insight into plate boundary deformation downdip of the locked seismogenic zone. We employ network autocorrelation detection to identify LFE families beneath southern Vancouver Island and environs. An initial suite of 5775 LFEs detected in 2004 and 2005 at a select set of 7 stations is grouped into 140 families using waveform cluster analysis. These families are used as templates within an iterative network cross correlation scheme to detect LFEs across different tremor episodes, incorporate new stations, and improve LFE template signal-to-noise ratio. As in southwest Japan, representative LFE locations define a relatively tight, dipping surface several km above the locus of intraslab seismicity, within a prominent, dipping low-velocity zone (LVZ). LFE polarizations for near-vertical source-receiver geometries possess a remarkably uniform dipolar signature indicative of point-source, double-couple excitation. Focal mechanisms determined from P-wave first motions are characterized by a combination of strike-slip and thrust faulting. We suggest that LFEs and regular intraslab seismicity occur in distinct structural and stress regimes. The LVZ, inferred to represent weak, overpressured, porous and mylonitized metabasalts of oceanic crustal Layer 2, separates LFEs manifesting deformation within a plate boundary shear zone from intraslab earthquakes generated by tensional stresses and dehydration embrittlement within a more competent lower oceanic crustal Layer 3 and underlying mantle.

1. Introduction

[2] Low frequency earthquakes (LFEs) are small ($M \leq 2$) events first identified by *Katsumata and Kamaya* [2003] as being associated with tectonic tremor [*Obara*, 2002] in southwest Japan. Like tremor, they are characterized by a frequency spectrum that is peaked between 1 and 10 Hz, and so are distinctly lower frequency than regular earthquakes of comparable magnitude. In some instances, both P- and S-wave times can be picked from LFE recordings leading to improved hypocentral depth determination over tremor location methods that rely on waveform envelopes. *Katsumata and Kamaya* [2003] noted that LFE locations determined from P- and S-times clustered in a narrow belt

near the top of the subducting Philippine Sea plate in the vicinity of the mantle wedge corner, and suggested that tremor generation is related to metamorphic dehydration reactions in the subducting plate. Using LFE template events and highly sensitive network correlation coefficients [*Gibbons and Ringdahl*, 2006] as discriminants for LFE detection, *Shelly et al.* [2007] demonstrated that a significant proportion of tremor in southwest Japan can be viewed as the superposition of many small LFEs. Moreover, these authors have also demonstrated that LFE mechanisms in Japan are consistent with shallow thrusting in the direction of plate motion [*Ide et al.*, 2007], that LFEs occur on a surface inferred to be the plate boundary near the top of a layer marked by high V_P/V_S ratios [*Shelly et al.*, 2006], and that LFEs, tremor, other phenomena related to episodic tremor and slip (ETS) [*Dragert et al.*, 2001; *Rogers and Dragert*, 2003] and slow earthquakes, in general, appear to follow a magnitude-duration scaling relation that is distinct from typical seismicity [*Ide et al.*, 2006].

[3] Although LFEs were originally identified on Japanese records through routine visual inspection by monitoring agencies [*Nishide et al.*, 2000; *Beroza and Ide*, 2011], their appearance on seismograms from the Cascadia subduction zone where ETS is also observed [*Rogers and Dragert*, 2003] is less obvious. Isolated examples have been presented [e.g., *Kao et al.*, 2009; *La Rocca et al.*, 2009] but their signal-to-noise ratio (SNR) levels are low and limit possibilities for use as waveform templates in network correlation studies. The compilation of an LFE catalogue in Cascadia would be useful in gaining further insight into the ETS phenomenon, for example, by enabling comparative study with results from Japan. *Brown et al.* [2008] describe an approach that exploits autocorrelations of tremor time series recorded at a network of stations to automatically identify LFEs. In a follow-up study [*Brown et al.*, 2009], they illustrated application of their method using 3-hour segments of data from 3 subduction zones, including Cascadia (southern Vancouver Island). In this paper, we are motivated by their approach to compile a suite of high SNR LFE templates to examine the nature of LFEs and tremor beneath southern Vancouver Island.

2. Data and Methodology

[4] The data employed in this study have been assembled from a range of sources and processed in two steps. In the network autocorrelation step, described below, we have used seismograms recorded during the 2004 (July 4–26) and 2005

(September 3–25) ETS episodes from POLARIS-BC [*Nicholson et al.*, 2005] stations TWBB, TSJB, TWKB, MGCB, KELB, and permanent stations PFB, LZB and PGC run by the Geological Survey of Canada (GSC). This grouping of "anchor" stations crosses southern Vancouver Island in a quasi-linear array with 5–10 km station spacing. For the network cross correlation step, we extend our data set to other stations shown in Figure 1 on southern Vancouver Island, the northern Olympic Peninsula and the Gulf and San Juan Islands, including other POLARIS-BC sites, permanent GSC installations, stations of the Pacific Northwest Seismic Network operated by the University of Washington (UW), and temporary EarthScope deployments (USArray and Plate Boundary Observatory). All data are organized into 24-hour long files, filtered between 1 and 10 Hz and resampled to 40 sps.
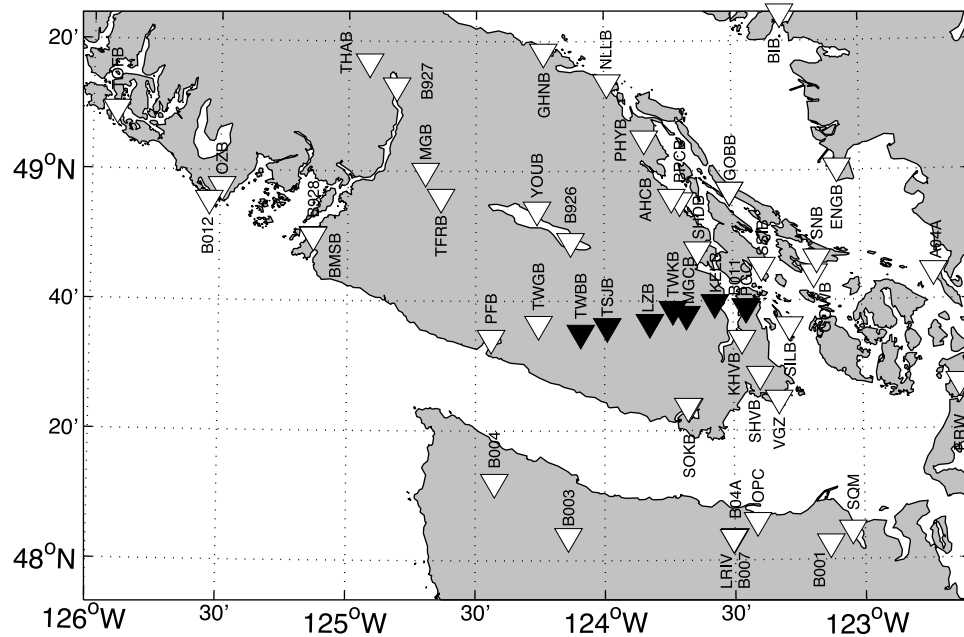
2.1. Network Autocorrelation

[5] To generate a suite of initial LFE detections we follow the general approach described by *Brown et al.* [2008] with some modification as summarized below. For each of the 7 three-component anchor stations listed above we divide each hour-long segment of data into 6-second long windows with 0.5 s overlap resulting in a total of 7188 windows per hour. Each window is correlated with all other windows within the same hour-long record and the results are stored as individual station/component autocorrelation records. Autocorrelation records from all stations and components corresponding to the same hour are summed to produce a network autocorrelation record. Detections are logged by searching for windows when the network autocorrelation exceeds a threshold of 8 times the median absolute deviation [*Shelly et al.*, 2006]. Since we restrict our search for repeat events to hour-long segments, we are not able to detect events that occur less than twice per hour.

[6] For the 46 days of tremor analyzed at the 7 stations for 2004 and 2005, we logged 5775 initial LFE detections. These initial detections were grouped into 140 families using a hierarchical cluster analysis [*Rowe et al.*, 2002] based on correlation coefficients of composite wave trains constructed by lining up all station/component records corresponding to an individual detection window.

2.2. Network Cross Correlation

[7] With initial detections grouped according to waveform similarity, we produced LFE templates by stacking all waveforms corresponding to a given station, component and initial detection family. These

Figure 1. Distribution of stations employed in this study (black triangles - anchor stations used in network autocorrelation step, white triangles - remaining stations incorporated in network cross correlation step).

templates were extended to include not only anchor stations but all stations operating during the 2004 and 2005 ETS intervals in the southern Vancouver Island region. Using subset templates comprising 6 or 7 stations, we proceeded to scan through tremor episodes in other years (2003, 2007–2011) by computing network cross correlation coefficient time series and logging times where this quantity again exceeds 8 times the median absolute deviation to assemble a new suite of detections, now associated with a given template. Selection of stations for the subset template is based on the SNR level of the template waveforms and, of course, the availability of station data for a given tremor episode. Since the stacked template waveforms possess significantly higher SNR than any of the initial detection waveforms, the network correlation procedure produces more detections than the network autocorrelations. Stations operating outside of the 2004 and 2005 ETS episodes were incorporated within the LFE template for a given family using detections within the appropriate recording period, allowing us to assemble a complete station complement. To improve both the number of detections and the SNR of the waveform templates, we adopted an iterative procedure of alternately i) performing LFE detection by network cross correlation with LFE templates, and ii) waveform stacking to update LFE templates. After 5 such iterations neither template SNR nor numbers of detections continued to show significant improvement. Most templates comprise between 1000–5000

independent detections made over the 8 ETS episodes although this number varies from station to station depending on data availability. In Figure 2 we present an example waveform template (# 176). Note that waveforms are impulsive, in particular those closest to the epicenter. *S*-wave arrivals dominate the response, especially on the horizontal components, but *P*-waves are also obvious in a majority of sections and at many stations on the vertical component.

3. LFE Template Location

[8] Since relative times are preserved within the waveform template, we may use *P*- and *S*-traveltime picks to generate a representative hypocentral location for each LFE family. Although some of the 140 composite waveform templates exhibit overlap in contributing detections, we will consider each template as representing a distinct LFE location. *P*- and *S*-wave first arrival times were picked from high SNR waveform templates, resulting in averages of approximately 16 *P*-times and 22 *S*-times per template. These times were inverted for location using the hypoinverse software distributed by the United States Geological Survey [*Klein*, 2002]. To facilitate comparison of LFE locations with a broader catalogue of GSC locations of regular earthquakes determined using a different algorithm, we also inverted GSC times (A. Bird, personal communication, 2012) for a small selection of these latter
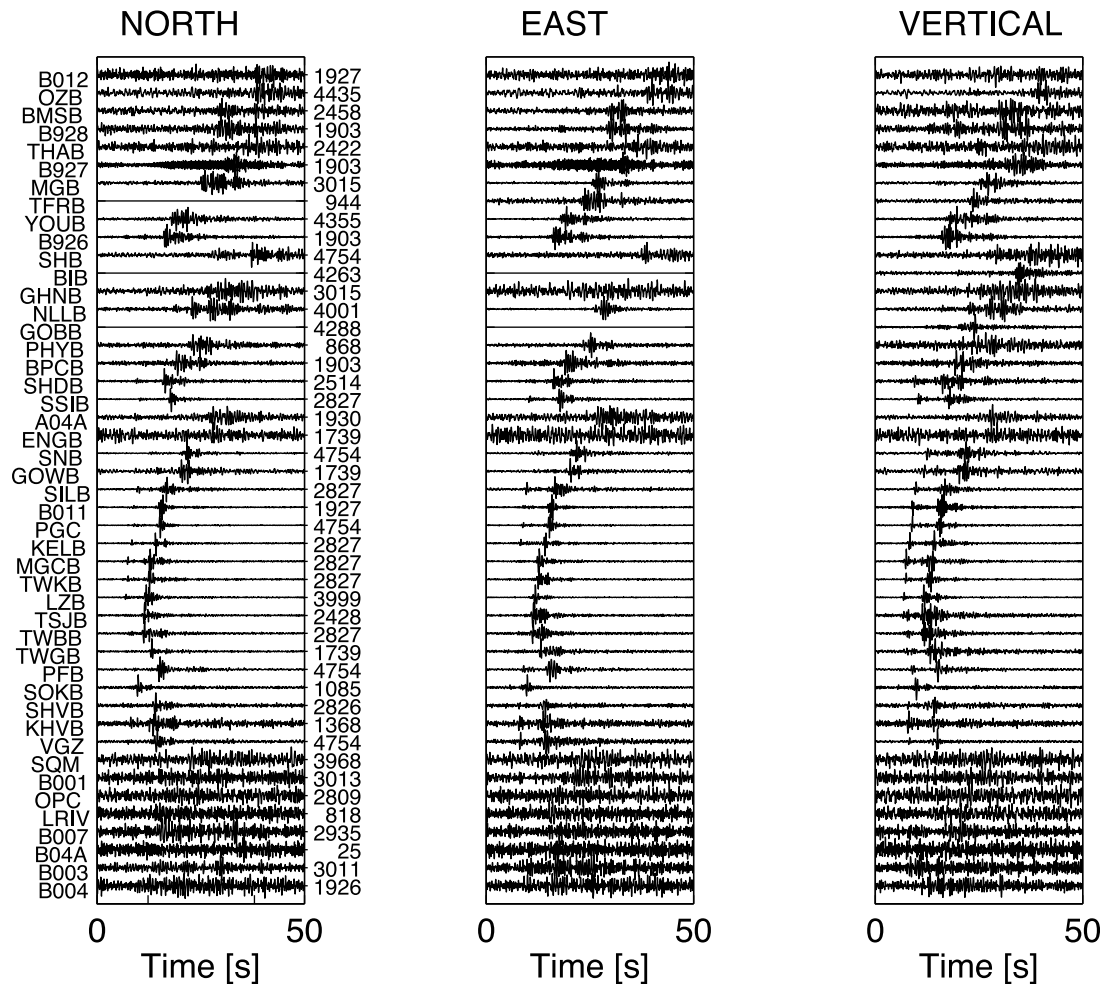
Figure 2. North, east and vertical LFE waveforms for template 176. Note impulsive waveforms for stations (SILB–PFB) closest to epicenter in southern Vancouver Island. SNR deteriorates across the Juan de Fuca Strait (SQM–B004) and toward central Vancouver Island (B012–B927). Numbers to right of north section indicate independent detections contributing to individual stations.

events to check that no significant biases were introduced through the use of different location algorithms and weighting parameters.

[9] In Figure 3, we display LFE epicenters on a map that also includes regular earthquake epicenters located between 1985–2012 from the GSC and UW catalogues. Data from the two catalogues were merged at the 48th parallel with a ±0.2° overlap and all duplicate events removed. The 20, 30 and 40 km depth contours to the top of subducting plate, as assembled by *Audet et al.* [2010] from 3-D modeling of receiver functions, are also plotted, together with locations of depth profiles A–A′, B–B′ and C–C′ shown in Figures 4, 5 and 8, respectively. In each of these profiles, LFEs and regular events falling within ±25 km of the profile axis are shown. The LFEs define a relatively tight

surface between 27 and 37 km depth approximately centered beneath the POLARIS-BC array. The concentration of LFE locations along strike is likely largely dictated by (and centered over) the distribution of anchor stations used for initial detection in the autocorrelation step as a result of diminishing SNR at greater distances. However, the dip distribution of LFE epicenters is largely bracketed by the anchor stations and furthermore coincides with high tremor densities mapped by *Kao et al.* [2009] and *Wech et al.* [2009].

4. LFE Waveform Polarizations

[10] We now consider the polarizations of *P*- and *S*-waveforms within the LFE templates, in particular, at stations located near the center of the LFE
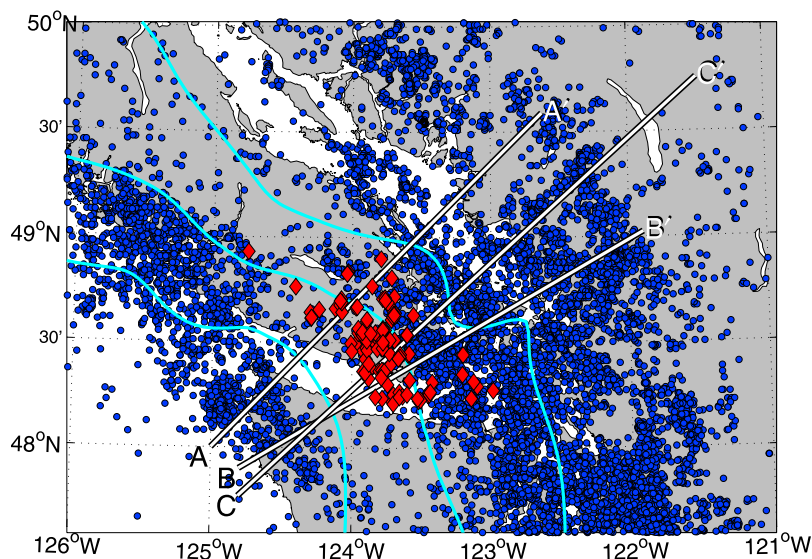
Figure 3. Map of seismicity in southern Vancouver Island region. Blue circles denote locations of regular (crustal and intraslab) earthquakes between 1985–2012, red diamonds are locations of LFE templates determined in this study from ETS episodes in 2003–2012. Cyan lines indicate the 20, 30 and 40 km depth contours to the top of the subducting Juan de Fuca plate as determined from receiver functions [*Audet et al.*, 2010]. Lines A–A′, B–B′ and C–C′ identify locations of profiles in Figures 4, 5, and 8, respectively.

distribution for which raypaths will tend to be closer to vertical, and so less likely to display phase distortions due to post-critical interactions with near-horizontal structure. In Figure 6 (top), we plot LFE template waveforms aligned on the east-component *S*-arrival and sorted according to epicentral distance for all 3 components at stations TWKB and LZB. *P*-component waveforms aligned on the vertical component at stations TWBB and PGC are shown in Figure 6 (bottom). The waveforms of both direct *S*- and *P*-arrivals remain remarkably uniform as functions of epicentral distance and comprise a "dipolar" wavelet. On the *S*-recordings this wavelet consists of negative followed by positive pulses on both north and east components. The direct *P*-arrival displays opposing vertical-component polarity at stations TWBB (positive followed by negative) and PGC (negative followed by positive) which lie updip and downdip, respectively, from the main cluster of LFE hypocenters in Figure 3. We have computed focal mechanism solutions from vertical component *P*-wave polarizations using the HASH software of *Hardebeck and Shearer* [2002] for a selection of LFE templates with clean *P*-arrivals. These solutions are shown in Figure 7 and consistently display a mixture of strike slip and thrust mechanisms. If the shallower nodal plane is identified with the fault plane, strike-slip motion has a left-lateral sense. Closer inspection of waveforms in Figure 6 yields evidence for a structural imprint. For example, there
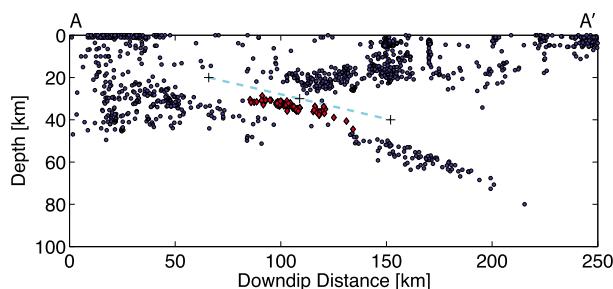
Figure 4. Depth profile A–A′ of seismicity across northern margin of LFE distribution. Dashed cyan lines represent quadratic fit to estimates of 20, 30 and 40 km depths (shown as +′s) to top of plate from *Audet et al.* [2010] model. Regular seismicity is shown as blue circles, LFEs as red diamonds.
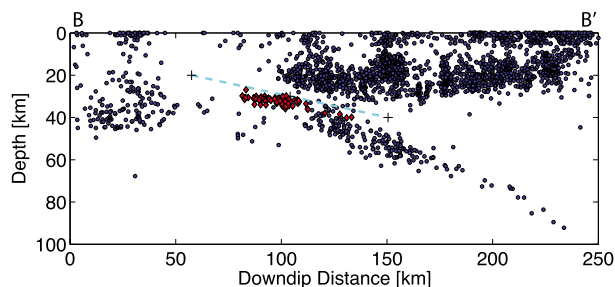
Figure 5. Depth profile B–B′ of seismicity across northern margin of LFE distribution. See Figure 4 for explanation.
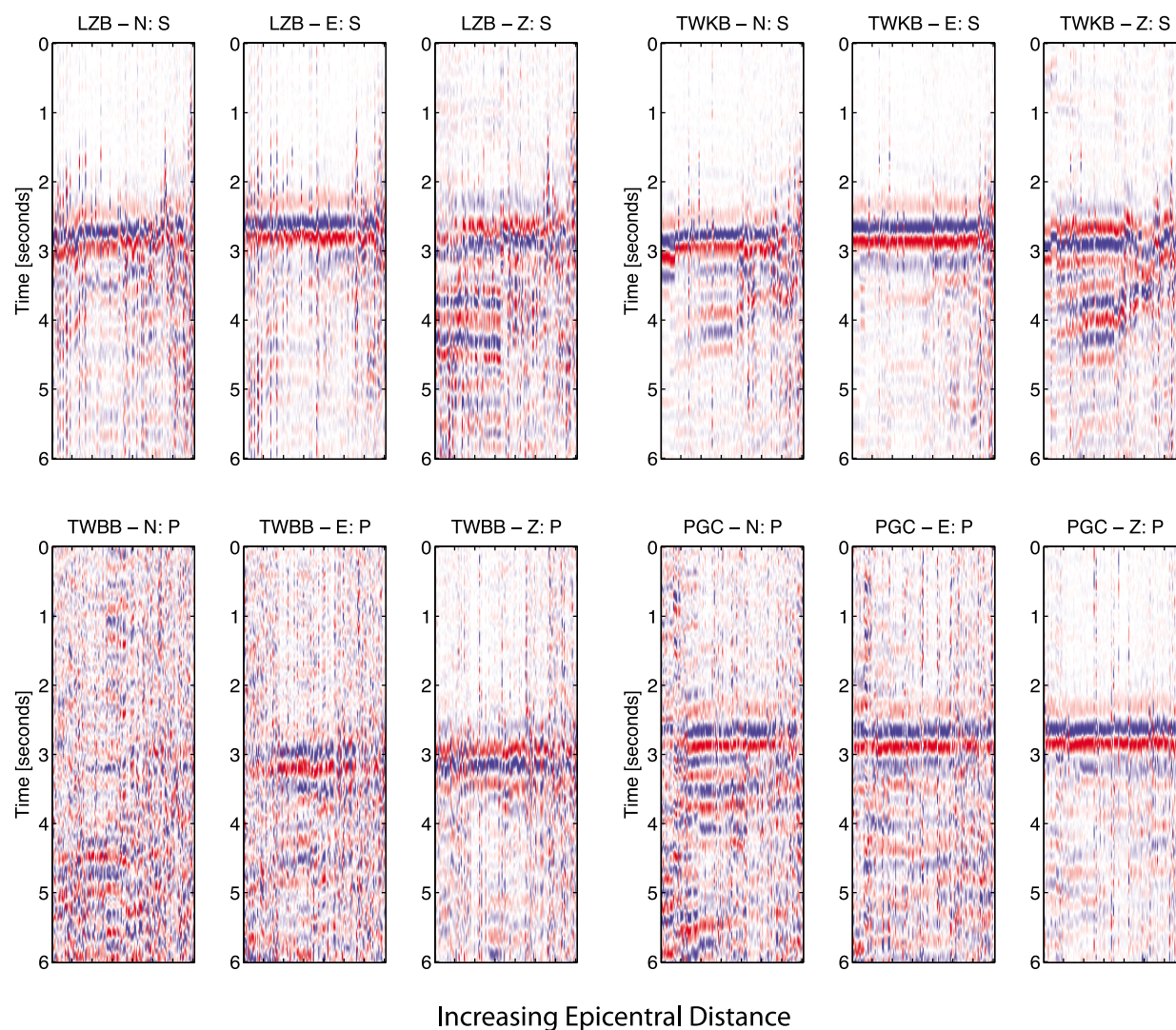
Figure 6. LFE polarizations. (top) LFE *S*-polarizations for 3-component stations LZB and TWKB. Waveforms are ordered in increasing epicentral distance and aligned on the *S*-waveform of the east component. Note uniform dipolar signature of direct *S* across all LFEs. (bottom) LFE *P*-polarizations for stations TWBB and PGC aligned on *P*-waveform of vertical component. Note opposing polarities for these two stations that are consistent with shallow thrust mechanisms.

appears to be systematic decrease in delay as a function of epicentral distance between north and east components of the *S*-arrival at station LZB that suggests *S*-wave splitting due to anisotropy. In addition, a number of coherent arrivals can be identified following both direct *P*- and *S*-arrivals with a well defined move out, and are likely scattered waves from strong, short-wavelength heterogeneity.

5. Discussion

[11] The compilation of a suite of LFE families for southern Vancouver Island allows a number of important constraints to be placed on the nature of

ETS in Cascadia. We begin by considering the spatial distribution of LFE hypocenters and its relation to regular seismicity. As evident in Figure 3, LFE epicenters fall between approximately the 25 and 37 km plate boundary depth contours as given in the *Audet et al.* [2010] model. The LFEs partly fill a gap formed by two prominent bands of seismicity: the first band skirts the west coast of Vancouver Island and the northern Olympic Peninsula, whereas the second band is centered over the Georgia Strait extending into Puget Sound [*Rogers and Crosson*, 2002]. The two bands possess representation in both crustal and intraslab earthquakes (see Figures 4 and 5). A complementarity in locations of tectonic tremor and regular earthquakes has been previously
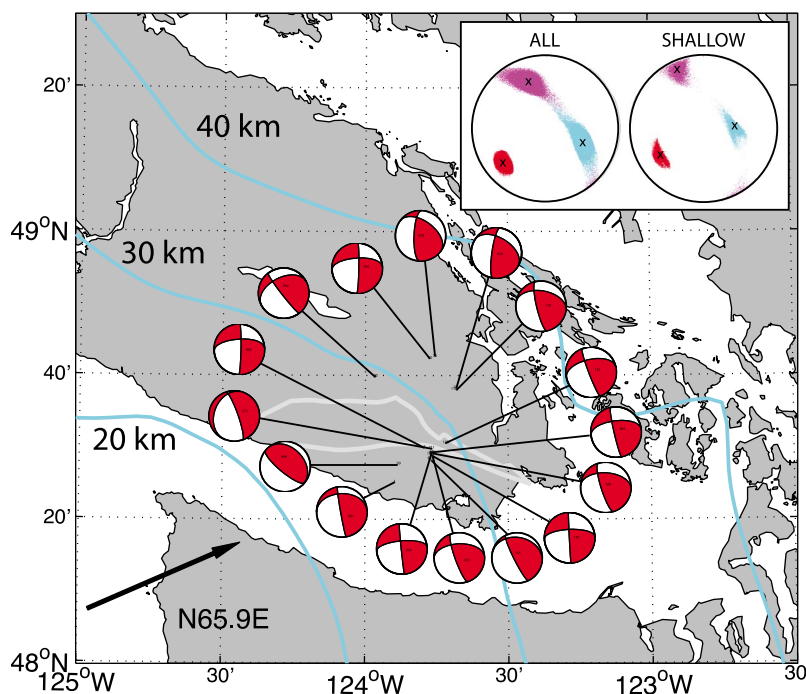
Figure 7. Focal mechanism solutions determined using *P*-wave first motions for a selection of LFE templates. Mechanisms tend to display a combination of thrust and strike slip motion. Juan de Fuca - southern Vancouver Island relative plate motion vector of N65.9E is computed from *McCaffrey et al.* [2007] and applies to location of station TWKB near center of LFE distribution (see Figure 1). Light grey lines delimit boundaries of Leech River Complex [*Cowan*, 2003]. Inset at upper right displays estimates of principal stress directions projected onto lower hemisphere determined using the method of *Michael* [1984] where (right) the shallowly dipping nodal plane is assumed to be the fault plane, and (left) both sets of planes are entered as fault planes within a duplicate data set. 95% confidence intervals are shown for the maximum (compressive, red), intermediate (magenta) and minimum (cyan) principal stresses determined from 10000 bootstrap samples.

noted in the Vancouver Island region [*Kao et al.*, 2005, 2009] as well as northern California and southern Oregon [*Boyarko and Brudzinski*, 2010]. Although there is some overlap in the downdip epicentral distribution of LFEs with regular seismicity, inspection of the depth profiles indicates that the two classes of earthquake are indeed spatially segregated. Along profile A–A′, the LFEs form a surface that lies approximately parallel to and 5–10 km below the main distribution of crustal earthquakes and a comparable distance above that of intraslab seismicity. Distinct hypocentral distributions along profile B–B′ are not quite so clearly defined, especially near the downdip end of the LFE distribution, but the LFEs again form a relatively tight surface that lies at or above the trajectory formed by the top of the Wadati-Benioff zone. Figures 4, 5, and 8 record the positions of the 20 km, 30 km, and 40 km slab depth contours as '+'s along the respective profiles from *Audet et al.* [2010] and, in dashed cyan lines, a quadratic fit to these points. The majority of LFEs lie below and within 5 km of this estimate of the plate boundary, and there is the suggestion that the discrepancy is

larger at shallower depths. More precisely, the LFE hypocenters fall between 0 and 7.7 km from the plate boundary with a mean of 4.0 km and standard deviation about the mean of 1.7 km.

[12] Figure 8 superposes seismicity distributions on a 2-D diffraction tomographic image of *S*-velocity perturbations across profile C–C′ determined using teleseismic *P*-receiver functions [*Nicholson et al.*, 2005]. The image is dominated by the presence of a dipping low-velocity zone (LVZ, in red) evident from the coast line (0 km distance, 20 km depth) to a depth of ∼37 km depth at 65 km distance. At greater depths, the upper contrast of the LVZ disappears, though its base persists with diminishing contrast to at least 70 km and roughly coincides with the locus of intraslab seismicity. The LVZ was interpreted by *Nicholson et al.* [2005] as the seismic expression of subducting oceanic crust, but more recent, detailed studies of its seismic properties and dimensions favor an explanation as upper oceanic crust [*Hansen et al.*, 2012; *Bostock*, 2012]. In particular, the LVZ is characterized by V_P/V_S ratios
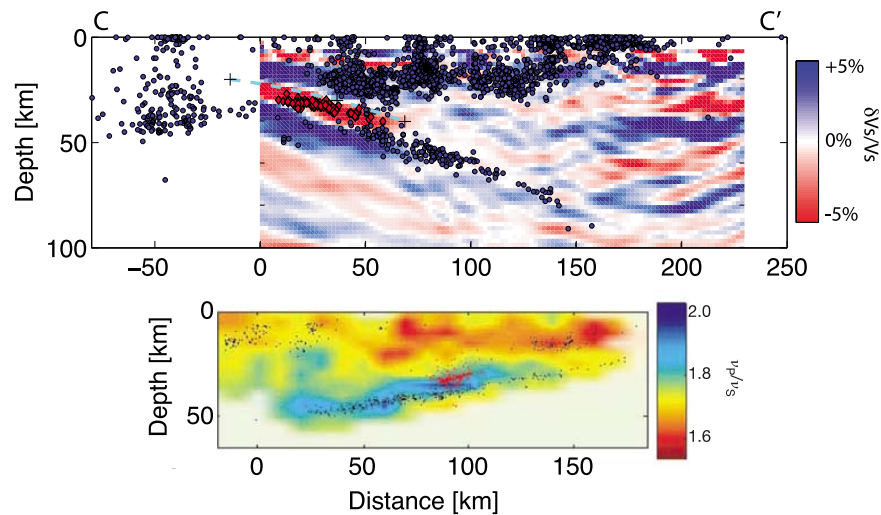
Figure 8. Comparison of profiles from (top) Vancouver Island (corresponding to line C–C′ in Figure 3, modified from *Nicholson et al.* [2005]) and (bottom) southwest Japan (modified from *Shelly et al.* [2006]). See Figure 4 for explanation of symbols in Figure 8 (top) and main text for explanation of diffraction tomography image. Image of southwest Japan displays variations in V_P/V_S with superposed LFEs (red dots) and regular seismicity (black dots).

near 2.4 and a thickness near 4 km (exaggerated in Figure 8 due to frequency band limitation and a reference velocity model that does not adequately describe the LVZ's extreme elastic properties [*Audet et al.*, 2009]). The LVZ is thought to result from near-lithostatic, pore fluid pressures generated through dehydration of metabasalts in oceanic crustal Layer 2, an impermeable seal along the plate boundary above [*Audet et al.*, 2009; *Peacock et al.*, 2011] and low-porosity metagabbro of the underlying lower oceanic crust (Layer 3). A second feature of note in the diffraction tomographic profile is the presence of the continental Moho at its landward end (C′) defined as the juxtaposition of lower velocity (red) crust with higher velocity (blue) mantle near 37 km, a depth consistent with the refraction estimates by *Zelt et al.* [1993]. The seismic expression of the continental Moho diminishes as one proceeds seaward of distance 150 km, an effect inferred to be due to hydration and serpentinization of the forearc mantle [*Bostock et al.*, 2002; *Hyndman and Peacock*, 2003; *Christensen*, 2004]. Note that the top of plate boundary defined by *Audet et al.* [2010] based on 3-D receiver function modeling of scattered waves from the LVZ corresponds closely to the top of LVZ in the diffraction image, suggesting that the 2-D image is not significantly contaminated by 3-D structure. As in Figures 4 and 5, the LFEs in Figure 8 lie below the plate boundary within the LVZ. They terminate near a depth of 37 km that coincides with the seaward extrapolation of the continental Moho at the northeastern edge of the profile, suggesting that composition of the overriding plate along the plate

boundary could influence their generation, perhaps through alteration of hydrological conditions [*Audet et al.*, 2009]. We also note, however, that although our LFE locations coincide closely with high tremor densities mapped by *Kao et al.* [2009] and *Wech et al.* [2009], some tremor is mapped landward of the LFEs.

[13] In Figure 8 (bottom), we reproduce Figure 4c from *Shelly et al.* [2006] that presents LFEs and intraslab seismicity atop a profile of V_P/V_S perturbations across Shikoku, as determined using double-difference traveltime tomography. The Cascadia and Nankai images are plotted to the same scale and a number of similarities and differences are evident. On both profiles LFEs occur a few km above the Wadati-Benioff zone, approaching the top of a high V_P/V_S layer. However, the downdip extent of LFE occurrence in Cascadia is significantly broader than at the Nankai location at 50 vs 20 km, and LFEs on the Shikoku cross section appear to terminate updip of a mantle wedge corner that, from receiver function studies [*Shiomi et al.*, 2004], is reached at approximately 40 km depth. This observation indicates that the downdip extent of LFEs in this region is not governed by the crust-to-mantle transition in the overriding plate. The vertical separation of LFEs and intraslab events suggests that the LVZ, interpreted here as upper oceanic crust, cannot support regular earthquakes perhaps owing to low shear strength induced by metamorphic dehydration and high pore fluid pressures, and that intraslab seismicity is concentrated within more competent

gabbroic and ultramafic material in the lower oceanic crust and upper mantle of the subducting plate [*Wang et al.*, 2004]. In this context, the increased proximity of LFEs and intraslab events near the downdip limit of LFEs (and prominent LVZ) on profile B–B′ could be explained as due to a transition to diminished pore fluid pressures and porosity. This transition, brought about by the onset of eclogitization and consequent compromise of the plate boundary seal [*Audet et al.*, 2009], could enable intraslab seismicity, originating through dehydration embrittlement [*Kirby et al.*, 1996], to extend into shallower levels of the oceanic crust at greater depths [cf. *Preston et al.*, 2003].

[14] The simplicity of direct *P*- and *S*-arrival waveforms in Figure 6 and, in particular their dipolar signature in particle velocity as measured in the far-field, imply point-source, double-couple excitation [e.g., *Shearer*, 2009]. That is, the LFE templates can be considered to represent empirical, time-differentiated Green's functions. Unlike Japan, where focal mechanisms appear to be dominantly shallow thrust in the direction of plate motion [*Ide et al.*, 2007], the solutions in Figure 7 consistently display a component of strike-slip motion. Slip vectors for earthquakes on the Cascadia thrust in this region should be slightly more easterly than the Juan de Fuca-North America relative plate motion vector (46.4 mm/yr N64°E at station TWKB near the center of the LFE distribution using values from Table 2 of *McCaffrey et al.* [2007]) because western North America is moving relative to a fixed North America reference frame. According to geodetically constrained block models and geological indicators [*McCaffrey et al.*, 2007], southern Vancouver Island moves at a rate of 3.2 mm/yr N43°E relative to North America; consequently the Cascadia slip rate vector is 43.5 mm/yr N66°E at station TWKB.

[15] The range of nodal planes represented in the focal mechanism solutions is sufficient to permit inversion for stress orientation under the assumption that stress is uniform over the region. We apply the stress inversion method of *Michael* [1984] to two data sets (see Figure 7, inset). In the first data set (labeled "ALL" in inset), each focal mechanism is represented twice, once for each nodal plane as the fault plane, thereby accounting for fault plane ambiguity [*Michael*, 1987]. The solution yields a maximum (compressive) principal stress axis oriented N51°E, plunging 27° to the southwest (point "X" in the red population reflecting 95% confidence area from 10000 bootstrap sample solutions). This value is approximately 15° more northerly than

the convergence vector, suggesting a contribution from margin-parallel compression (as in the upper crust [e.g., *Wang*, 2000]). The other two principal stress axes are poorly constrained (intermediate stress in magenta, minimum stress in cyan), indicating either comparable magnitudes or local stress variations. In the second inversion ("SHALLOW" in inset), the shallower of the 2 nodal planes is taken to be the fault plane based on the assumption that deformation manifest by LFEs should preferentially align with the subhorizontal attitude of subduction. This solution presents a maximum compressive stress oriented at N59°E plunging 32° to the southwest with well defined intermediate and minimum principal stress axes. The stress state within the LVZ implied by this analysis is broadly consistent with thrust faulting along planes subparallel to the subduction interface, but left-lateral faulting on planes striking east-west planes or right-lateral strike-slip faulting on north-south planes, are also consistent with this stress state. A diversity in available frictional slip plane orientations may account for the variable LFE focal mechanisms on Figure 7.

[16] This picture is again consistent with the notion of the LVZ as a weak, frictional-viscous shear zone with frictional slip occurring on a variety of brittle surfaces [e.g., *Handy et al.*, 1999]. Given the presence of pore fluids, likely development of phyllosilicate minerals in situ, and large total shear strains, a dramatically weakened, clastomylonite shear zone may exist from the subduction interface into the upper oceanic crust. LFEs likely represent brittle failure of local patches within this dominantly ductile shear zone, within or between pods of competent material [e.g., *Fagereng and Sibson*, 2010; *Nakata et al.*, 2011]. The well developed shear fabric would reduce shear strength for both brittle and ductile deformation [*Niemeijer et al.*, 2010]. Large strains associated with subduction (including slow slip events) are accommodated by ductile flow along mylonite strands, whereas local brittle patches may be loaded by both this ductile flow and upper plate stresses to produce LFEs.

[17] The stress field within the LVZ is thus distinct from that inferred from deeper intraslab events that exhibit slab-normal compression and down-dip tension [*Wada et al.*, 2010], and from shallow crustal seismicity characterized by north-south compression [e.g., *Ma et al.*, 1996; *Wang*, 2000] (cf. Figure 7, inset). This variation in stress state suggests that the LVZ behaves as a decoupling horizon operating at low differential stresses.
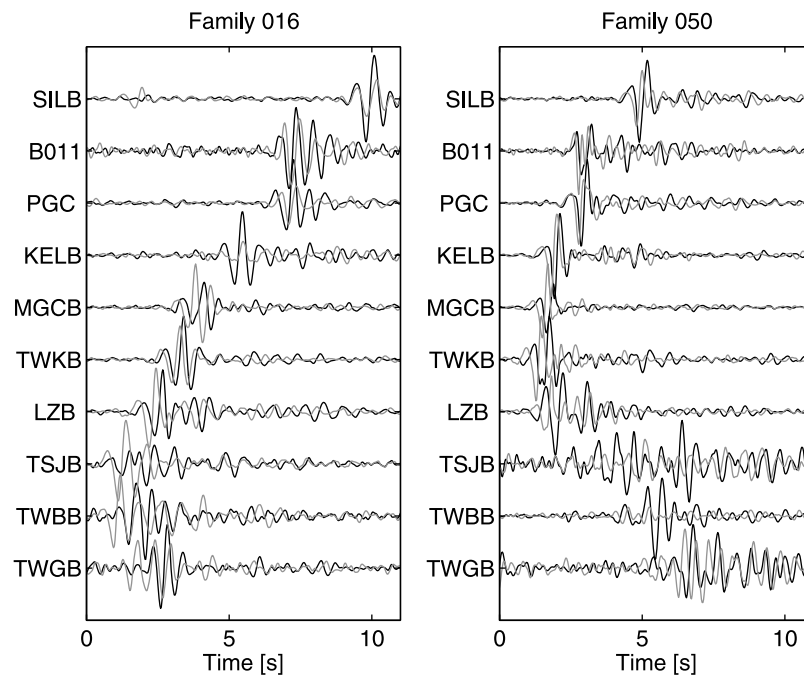
Figure 9. Horizontal component waveforms for LFE templates 016 and 050. The east component (grey) tends to lead the north component (black) with delays up to 0.3 s at stations LZB and TWK and perhaps more severe waveform distortion at stations TSJB, TWBB, TWKB manifesting the presence of strong crustal anisotropy [*Bostock and Christensen*, 2012].

[18] It is notable that a significant fraction of the stations along the POLARIS-BC line sit astride or in close proximity to the San Juan fault, the northern boundary of the Leech River Schist [*Cowan*, 2003]. Previous work [*Bostock and Christensen*, 2012] employing raw tremor waveforms has demonstrated the presence of significant *S*-wave splitting of up to 0.3 s in signals from these stations. Horizontal component waveforms at stations LZB and TWKB, shown in Figure 6, corroborate this finding in demonstrating a consistent phase advance of east component over north component for a broad range of epicentral distances. Note in particular, that the advance systematically diminishes with increasing epicentral distance at station LZB. Figure 9 displays north and east components of the direct *S*-arrival for a subset of stations crossing southern Vancouver Island for LFE templates 016 and 050. Varying degrees of splitting are evident for stations SILB-LZB whereas waveform distortion appears to become still more severe at western stations TSJB, TWBB and TWGB. Laboratory measurements of velocity from samples taken from the Leech River schist display some of the strongest *S*-anisotropy (30%) yet measured for low grade metamorphic rocks, providing a compelling example for an origin of crustal anisotropy in lattice preferred orientation of phyllosilicate minerals [*Bostock and Christensen*, 2012].

[19] The second structural signal evident in Figure 6 in the form of additional phases following the primary *P*- and *S*-arrivals, is likely related to short-wavelength, structural heterogeneity. In particular, the timing of phases at smaller epicentral distances is consistent with an origin in reflection/conversion from the base of the LVZ in Figure 8. We are currently investigating this possibility. The timing of scattered phases from boundaries of the LVZ would provide a powerful means of precisely mapping LFE location relative to the LVZ and gaining further insight into the nature of LFEs and tectonic tremor.

6. Conclusions

[20] We have employed network autocorrelation and cross correlation to assemble a set of LFE templates for southern Vancouver Island. As in Japan, LFEs define a surface that lies several km above intraslab seismicity within a pronounced LVZ, interpreted here as upper oceanic crustal Layer 2 (+/− Layer 1 sediments). LFE template waveforms in particle velocity representing near-vertical propagation paths reveal a remarkably uniform dipolar signature indicative of point-source, double-couple excitation. Focal mechanisms for a select set of LFE templates display a combination of thrust and strike slip faulting

that manifests a maximum compressive stress plunging shallowly to the southwest. This stress state contrasts with north–south compression that characterizes the overriding plate and the slab-normal compression and downdip tension documented for intraslab events. Our observations are consistent with the notion that plate boundary deformation is distributed within a weak, overpressured, porous and mylonitized upper oceanic crust that enables a decoupling of stress regimes.

Acknowledgments

References

Audet, P., M. G. Bostock, N. I. Christensen, and S. M. Peacock (2009), Seismic evidence for overpressured subducted oceanic crust and megathrust sealing, *Nature*, *457*, 76–78.

Audet, P., M. G. Bostock, D. C. Boyarko, M. R. Brudzinski, and R. M. Allen (2010), Slab morphology in the Cascadia fore arc and its relation to episodic tremor and slip, *J. Geophys. Res.*, *115*, B00A16, doi:10.1029/2008JB006053.

Beroza, G. C., and S. Ide (2011), Slow earthquakes and nonvolcanic tremor, *Annu. Rev. Earth Planet. Sci.*, *39*, 271–296.

Bostock, M. G. (2012), The Moho in subduction zones, *Tectonophysics*, doi:10.1016/j.tecto.2012.07.007, in press.

Bostock, M. G., and N. I. Christensen (2012), Split from slip and schist: Crustal anisotropy beneath northern Cascadia from non-volcanic tremor, *J. Geophys. Res.*, *117*, B08303, doi:10.1029/2011JB009095.

Bostock, M. G., R. D. Hyndman, S. Rondenay, and S. M. Peacock (2002), An inverted continental Moho and serpentinization of the forearc mantle, *Nature*, *417*, 536–538.

Boyarko, D. C., and M. R. Brudzinski (2010), Spatial and temporal patterns of nonvolcanic tremor along the southern Cascadia subduction zone, *J. Geophys. Res.*, *115*, B00A22, doi:10.1029/2008JB006064.

Brown, J. R., G. C. Beroza, and D. R. Shelly (2008), An autocorrelation method to detect low frequency earthquakes within tremor, *Geophys. Res. Lett.*, *35*, L16305, doi:10.1029/2008GL034560.

Brown, J. R., G. C. Beroza, S. Ide, K. Ohta, D. R. Shelly, S. Y. Schwartz, W. Rabbel, M. Thorwart, and H. Kao (2009), Deep low frequency earthquakes in tremor localize to the plate interface in multiple subduction zones, *Geophys. Res. Lett.*, *36*, L19306, doi:10.1029/2009GL040027.

Christensen, N. I. (2004), Serpentinites, peridotites, and seismology, *Int. Geol. Rev.*, *46*, 795–816.

Cowan, D. S. (2003), Revisiting the Baranof-Leech River hypothesis for early Tertiary coastwise transport of the Chugach-Prince William terrane, *Earth Planet. Sci. Lett.*, *213*, 463–475.

Dragert, H., K. Wang, and T. S. James (2001), A silent slip event on the deeper Cascadia subduction interface, *Science*, *292*, 1525–1528.

Fagereng, Å., and R. H. Sibson (2010), Melange rheology and seismic style, *Geology*, *38*, 751–754.

Gibbons, S. J., and F. Ringdal (2006), The detection of low magnitude seismic events using array-based waveform correlation, *Geophys. J. Int.*, *165*, 149–166.

Handy, M., S. Wissing, and L. Streit (1999), Frictional-viscous flow in mylonite with varied bimineralic composition and its effect on lithospheric strength, *Tectonophysics*, *303*, 175–191.

Hansen, R. T. J., M. G. Bostock, and N. I. Christensen (2012), Nature of the low velocity zone in Cascadia from receiver function waveform inversion, *Earth Planet. Sci. Lett.*, *337–338*, 25–38.

Hardebeck, J. L., and P. M. Shearer (2002), A new method for determining first-motion focal mechanisms, *Bull. Seismol. Soc. Am.*, *92*, 2264–2276.

Hyndman, R. D., and S. M. Peacock (2003), Serpentinization of the forearc mantle, *Earth Planet. Sci. Lett.*, *212*, 417–432.

Ide, S., G. C. Beroza, D. R. Shelly, and T. Uchide (2006), A scaling law for slow earthquakes, *Nature*, *447*, 76–79.

Ide, S., D. R. Shelly, and G. C. Beroza (2007), The mechanism of deep low frequency earthquakes: Further evidence that deep nonvolcanic tremor is generated by shear slip on the plate interface, *Geophys. Res. Lett.*, *34*, L03308, doi:10.1029/2006GL028890.

Kao, H., S.-J. Shan, H. Dragert, G. Rogers, J. F. Cassidy, and K. Ramachandran (2005), A wide depth distribution of seismic tremors along the northern Cascadia margin, *Nature*, *436*, 841–844, doi:10.1038/nature03903.

Kao, H., S.-J. Shan, H. Dragert, and G. Rogers (2009), Northern Cascadia episodic tremor and slip: A decade of tremor observations from 1997 to 2007, *J. Geophys. Res.*, *114*, B00A12, doi:10.1029/2008JB006046.

Katsumata, A., and N. Kamaya (2003), Low-frequency continuous tremor around the Moho discontinuity away from volcanoes in the southwest Japan, *Geophys. Res. Lett.*, *30*(1), 1020, doi:10.1029/2002GL015981.

Kirby, S. H., E. R. Engdahl, and R. Denlinger (1996), Intraslab earthquakes and arc volcanism: Dual physical expressions of crustal and uppermost mantle metamorphism in subducting slabs, in *Subduction: Top to Bottom*, *Geophys. Monogr. Ser.*, vol. 96, edited by G. E. Bebout et al., pp. 195–214, AGU, Washington, D. C.

Klein, F. W. (2002), User's guide to Hypoinverse-2000, a FORTRAN program to solve for earthquake locations and magnitudes, *U.S. Geol. Surv. Open File Rep.*, *02-171*.

La Rocca, M., K. C. Creager, D. Galluzzo, S. Malone, J. E. Vidale, J. R. Sweet, and A. G. Wech (2009), Cascadia tremor located near plate interface constrained by S minus P wave times, *Science*, *323*, 620–623.

Ma, L., R. Crosson, and R. Ludwin (1996), Western Washington earthquake focal mechanisms and their relationship to regional tectonic stress, *U.S. Geol. Surv. Prof. Pap.*, *1560*, Part 1, 256–283.

McCaffrey, R., A. Qamar, R. King, R. Wells, G. Khazaradze, C. Williams, C. Stevens, J. Vollick, and P. Zwick (2007), Fault locking, block rotation and crustal deformation in the Pacific Northwest, *Geophys. J. Int.*, *169*, 1315–1340, doi:10.1111/j.1365-246X.2007.03371.x.

Michael, A. J. (1984), Determination of stress from slip data: Faults and folds, *J. Geophys. Res.*, *89*, 11,517–11,526.

Michael, A. J. (1987), Use of focal mechanisms to determine stress: A control study, *J. Geophys. Res.*, *92*, 357–368.

Nakata, R., R. Ando, T. Hori, and S. Ide (2011), Generation mechanism of slow earthquakes: Numerical analysis based on a dynamic model with brittle-ductile mixed fault heterogeneity, *J. Geophys. Res.*, *116*, B08308, doi:10.1029/2010JB008188.

Nicholson, T., M. G. Bostock, and J. F. Cassidy (2005), New constraints on subduction zone structure in northern Cascadia, *Geophys. J. Int.*, *161*, 849–859.

Niemeijer, A., C. Marone, and D. Elsworth (2010), Fabric-induced weakness of tectonic faults, *Geophys. Res. Lett.*, *37*, L03304, doi:10.1029/2009GL041689.

Nishide N., et al. (2000), Nationwide activity of low-frequency earthquakes in the lower crust in Japan, abstract Sk-P002 presented at Japan Earth and Planetary Science Joint Meeting, Geod. Soc. of Jpn., Tokyo.

Obara, K. (2002), Nonvolcanic deep tremor associated with subduction in southwest Japan, *Science*, *296*, 1679–1681.

Peacock, S. M., N. I. Christensen, M. G. Bostock, and P. Audet (2011), High pore pressures and porosity at 35 km depth in the Cascadia subduction zone, *Geology*, *39*, 471–474, doi:10.1130/G31649.1.

Preston, L. A., K. C. Creager, R. S. Crosson, T. M. Brocher, and A. M. Tréhu (2003), Intraslab earthquakes: Dehydration of the Cascadia slab, *Science*, *302*, 1197–1200.

Rogers, G. C., and R. S. Crosson (2002), Intraslab earthquakes beneath Georgia Strait/Puget Sound, in *The Cascadia Subduction Zone and Related Subduction Systems*, edited by S. Kirby et al., *U.S. Geol. Surv. Open File Rep.*, *02-328*, 65–67.

Rogers, G., and H. Dragert (2003), Episodic tremor and slip on the Cascadia Subduction Zone: The chatter of silent slip, *Science*, *300*, 1942–1943.

Rowe, C. A., R. C. Aster, B. Borchers, and C. J. Young (2002), An automatic, adaptive algorithm for refining phase picks in large seismic data sets, *Bull. Seismol. Soc. Am.*, *92*, 1660–1674.

Shearer, P. M. (2009), *Introduction to Seismology*, 396 pp., Cambridge Univ. Press, Cambridge, U. K.

Shelly, D. R., G. C. Beroza, S. Ide, and S. Nakamura (2006), Low-frequency earthquakes in Shikoku, Japan, and their relationship to episodic tremor and slip, *Nature*, *442*, 188–191.

Shelly, D. R., G. C. Beroza, and S. Ide (2007), Non-volcanic tremor and low-frequency earthquake swarms, *Nature*, *446*, 305–307.

Shiomi, K., H. Sato, K. Obara, and M. Ohtake (2004), Configuration of subducting Philippine Sea plate beneath southwest Japan revealed from receiver function analysis based on the multivariate autoregressive model, *J. Geophys. Res.*, *109*, B04308, doi:10.1029/2003JB002774.

Wada, I., S. Mazzotti, and K. Wang (2010), Instraslab stresses in the Cascadia Subduction Zone from inversion of earthquake focal mechanisms, *Bull. Seismol. Soc. Am.*, *100*, 2002–2013, doi:10.1785/0120090349.

Wang, K. (2000), Stress-strain 'paradox', plate coupling, and forearc seismicity at the Cascadia and Nankai subduction zones, *Tectonophysics*, *319*, 321–338.

Wang, K., J. F. Cassidy, I. Wada, and A. J. Smith (2004), Effects of metamorphic crustal densification on earthquake size in warm slabs, *Geophys. Res. Lett.*, *31*, L01605, doi:10.1029/2003GL018644.

Wech, A. G., K. C. Creager, and T. I. Melbourne (2009), Seismic and geodetic constraints on Cascadia slow slip, *J. Geophys. Res.*, *14*, B10316, doi:10.1029/2008JB006090.

Zelt, B. C., R. M. Zelt, and R. M. Clowes (1993), Crustal velocity structure in the eastern Insular and southernmost Coast belts, Canadian Cordillera, *Can. J. Earth Sci.*, *30*, 1014–1027.